A Microfacet-based Model for Photometric Stereo with General Isotropic Reflectance

Lixiong Chen, Yinqiang Zheng, Boxin Shi, Art Subpa-asa, and Imari Sato

Abstract—This paper presents a precise, stable, and invertible reflectance model for photometric stereo. This microfacet-based model is applicable to all types of isotropic surface reflectance, covering cases from diffusion to specular reflections. We introduce a single variable to physically quantify the surface smoothness, and by monotonically sliding this variable between 0 and 1, our model enables a versatile representation that can smoothly transform between an ellipsoid of revolution and the equation for Lambertian reflectance. In the inverse domain, this model offers a compact and physically interpretable formulation, for which we introduce a fast and lightweight solver that allows accurate estimations for both surface smoothness and surface shape. Finally, extensive experiments on the appearances of synthesized and real objects evidence that this model is state-of-the-art in our off-the-shelf solution.

Index Terms—photometric stereo, reflectance model, microfacet theory.

---◆---

1 INTRODUCTION

THE object appearance is quantified by the directional radiance that simultaneously encodes illumination, surface reflectance and object shape. Under a directional and calibrated light $\vec{l}$, the radiance of a surface measured from direction $\vec{v}$ is described as $I(\vec{l}, \vec{n}, \rho(\vec{v}, \vec{l}, \vec{n}))$, a quantity involving the highly nonlinear Bidirectional Reflectance Distribution Function (BRDF) $\rho(\cdot)$, which is usually defined case by case according to surface reflectance properties. For photometric stereo, inferring $\vec{n}$ and BRDF from I imposes challenges in a dimension that is never defined by photorealistic rendering. After all, complex models may enable flexible representations for rendering, but they never guarantee numerical feasibility in the inverse domain.

For two reasons the present-day photometric stereo still demands a versatile and invertible reflectance model. First, despite the successes achieved in recovering the shape of rough surfaces [1], [2], [3], few solutions exist to address general isotropic reflectance encompassing both diffusion and specular reflections, as exemplified in Figure 1. In fact, in the inverse domain a unified theory directly quantifying the formation of object appearance is still underdeveloped. Second, although emerging data-driven approaches [4], [5], [6] enable an end-to-end mapping from an object's appearance directly back to its shape, without a grounded explanation about the interplay between light and surface, their performance are at best achieved by immoderate consumption of computation and storage. Additionally, since existing work interprets surface reflectance algebraically rather than physically, a unified approach to coherent material and shape estimations is still awaiting investigations.

We note that, the microfacet theory [7], [8] avail us in

(a) aluminium   (b) green metallic paint   (c) white fabric

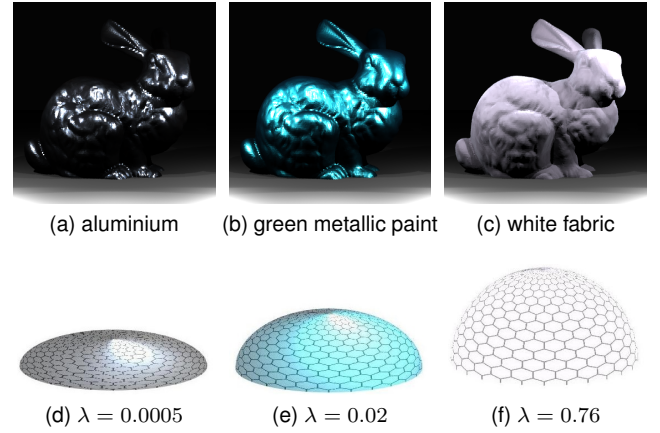(d) $\lambda = 0.0005$ (e) $\lambda = 0.02$ (f) $\lambda = 0.76$

Fig. 1: Object appearances displaying general isotropic reflectance are pervasive in the real world. This paper presents an effective approach to estimating the object shape and surface reflectance using microfacet-based reflectance model, covering cases including highly specular reflectance (a) "aluminium", specular reflectance (b) "green metallic paint" and diffusions (c) "white fabric". λ is the estimation for surface smoothness by our method. (d), (e) and (f) illustrate how λ models materials using the re-arranged distribution of the orientations of microfacets.

achieving both versatility and invertibility. First, it has full-fledged explanations about the formation of highly specular reflectance [9], hence it shall be well-extended to describe general reflectance [10]; second, its entire constructions are derived on the Normal Distribution Function (NDF) [11], [12], which often has a compact representation. However, these models in their current form lack a warrant for invertibility, let alone their portability to photometric stereo.

In this paper, we introduce a microfacet-based reflectance model that is serviceable for photometric stereo of general isotropic reflectance. We examine the state-of-the-

- L. Chen, Y. Zheng, A. Subpa-asa, and I. Sato are with National Institute of Informatics, Tokyo, 101-0003, Japan.
- B. Shi (corresponding author) is with the National Engineering Laboratory for Video Technology, School of Electronics Engineering and Computer Science, Peking University, Beijing, 100871, China. E-mail: shiboxin@pku.edu.cn.

art microfacet theory involving the ellipsoid microfacet normal distribution function (a.k.a. ellipsoid NDF), and have succeeded in deriving an invertible analytical model. The proposed model directly encodes the surface smoothness into a single variable $\lambda \in (0, 1]$, with $\lambda \to 0$ indicating the perfect mirror surface and $\lambda = 1$ representing an extremely rough surface that produces Lambertian reflectance. Geometrically, it controls the elongation of an ellipsoid depicting the distribution of the microfacets, which enables graceful transformation between a sphere and a flat disk. For $\lambda \to 0$, we introduce an approximation with appealing algebraic properties that estimates surface normal directly using highly specular reflectance, and we show that calibrated photometric stereo for highly specular surface in essence is to fit an ellipsoid of revolution, for which we have a fast, non-iterative and globally optimal solver. For the general isotropic reflectance with $\lambda \in (0, 1]$, we introduce an iterative solver, which we show outperforms the models developed under the extreme settings of $\lambda \to 0$ or $\lambda = 1$.

To sum up, this paper addresses photometric stereo of general isotropic reflectance, and it significantly extends our previous work reported in [13], which solves the case of specular reflectance only. Our contributions include:

1) Deriving an analytical, invertible, highly compact and generel isotropic reflectance model based on microfacet theory.
2) Designing a globally optimal solver that directly leverages surface smoothness for photometric stereo of highly specular reflectance.
3) Presenting an effective solution for photometric stereo of general isotropic reflectance that delivers state-of-the-art performance, and a training-free solution that demands much less computation and memory usage than the data-driven approaches do.

The remaining of this paper is organized as follows: Section 2 discusses the related works, Section 3 presents our analytical microfacet reflectance model, and its reduction for highly specular reflectance is derived in Section 3.5. Section 4 explains our normal recovery algorithm, then in Section 5 we showcase our experimental results. Section 6 concludes this paper by discussing the limitations of our solution.

2 RELATED WORKS

This section reviews existing work in two separate but converging domains: (1) BRDF design for photo-realistic rendering; (2) calibrated photometric stereo. The former studies appearance modeling of an object whose geometry is known, with a focus centered around modeling and acquisition; the latter infers the geometry of an object from its appearance, hence its related work is mostly on numerical and algorithmic implementations.

2.1 BRDF modeling

A BRDF accounts for the interaction between incident light and matter by evaluating the power distribution of reflected light in space. The finer the reflectance variation a BRDF is able to describe, the better the performance it offers. BRDFs can be categorized into two types: (1) empirically derived reflectance models and (2) physical-based reflectance models.

2.1.1 Empirically derived reflectance model

Empirical models are devised directly from observations. Namely, they provide a simple and intuitive formulation to conform observers' perception about surface reflection. These models are in general parameterized by a small set of variables without conforming to physics. Common empirical BRDFs are expressed in terms of a set of angles: $\vec{v}^\intercal \vec{l}$, the angle made between the light $\vec{l}$ and the viewing angle $\vec{v}$ [14]; $\vec{n}^\intercal \vec{h}$, the angle involving angular bisector $\vec{h}$ between light and view with the surface normal $\vec{n}$ [15]. Together with $\vec{v}^\intercal \vec{n}$ and $\vec{l}^\intercal \vec{n}$, they are the fundamental building blocks other more complex constructions. A typical way to express highly localized specular reflectance is to superimpose higher order polynomials [16], [17]. Since the formulation is motivated directly by perception, energy conservation is not enforced. Consequently, the rendered effects are largely dependent on parameter tuning.

2.1.2 Physically-based reflectance model

The microfacet-based BRDFs represent a type of model that conforms to physics. One common postulation made by these models is that the surface consists of randomly disposed facets, and the way each facet reflects the incident light is dictated by the law of electromagnetic. Depending on the size of the facet relative to the wavelength of the incident light, the aggregated reflectance can be simulated either by geometric optics [7], [18] or wave optics [9], [19], and it can also model surface smoothness [20]. The microfacet-based BRDF is mainly characterized by its normal distribution function (NDF), which specifies how microfacets are statistically distributed with respect to their orientations. Typical examples of NDF include Gaussian [21] or Beckmann distribution [22], followed by more complicated designs proposed recently [12], [23], [24]. NDF is an fundamental construction in describing surface reflectance, hence for rendering it is usually left as a design choice. A well-designed formulation is critical for photo-realistically rendering scenes of highly specular reflectance [25], [26].

2.1.3 Data acquisition for BRDF measurements

A relevant line of research proposes to tabulate BRDF directly. After all, a renderer's performance is often more important than its memory efficiency. While data acquisition advocates for dense sampling [27], [28], [29], subsequent studies show that directly bookkeeping the measurements is unnecessary, as real world BRDFs reside on a low dimensional manifold [30], [31], hence they can be decomposed into several low dimensional representations [10], [32]. In the context of microfacet theory, these low dimensional embeddings are closely-tied with the NDF, masking-shadowing function [33] and the Fresnel term [34], respectively.

In a factorable microfacet-based BRDF, NDF is the dominating factor [23] that can be well-parameterized. Parameters are determined through model fitting with measurements. Particularly, in our work we choose the ellipsoid NDF [35] to be our model, which in case of isotropic reflectance, is analogous to GGX/Trowbridge-Reitz distribution [11], [36]. Dense samples are always desired for fitting [37], and it can be achieved when the geometry of the

material sample is regular and known (e.g. a flat surface) [9]. Operation-wise, appearance sampling in this scenario draws some analogies to calibrated photometric stereo.

2.2 Photometric stereo under calibrated illumination

Photometric stereo defines an inverse problem for rendering. It utilizes appearance variation caused by illumination change to infer surface orientation. Unlike shape from shading (SFS) that takes a single image [38], photometric stereo assumes that lighting varies sufficiently so that the surface normal can be unambiguously determined [39]. The minimum number of required images, however, depends on reflectance property and shape complexity [40], [41], [42]. Low dimensional linear representations do not apply to shiny appearances, but if specularities are sparse, they could be discarded through outlier rejection [43], [44], [45]. The general reflectance could also be modeled by parametric BRDF models [1], [2], [46], or an algebraic composition of multiple parameterized components [3], [47].

Recent works adopt non-parametric or semi-parametric formulation to handle a broader range of materials. In these examples, only general reflectance properties, such as similarity [48], isotropy [49], monotonicity [50], visibility [51] and variation in spectral domain [52], [53] are taken as visual cues to constrain surface orientation. Moreover, the BRDFs can also be explicitly represented as a bivariate function [54], [55], a constrained bivariate regression [56] or a sparse dictionary-based representation [5]. BRDF designed for photometric stereo is a careful trade off between generality and complexity. Recently, emerging data-driven approaches [4], [5], [6] implement an end-to-end mapping that directly relates object appearances to surface normal, but these constructions only dedicated to a fixed illumination pattern, hence at current stage of their development they are highly inflexible. One recent work [57] attempts to remove this restriction by introducing an additional image synthesizer as to conform to the basic laws of reflectance, but this hybrid approach requires careful tuning on its intricate neural net implementation. Benchmark evaluation [58] demonstrates that more accurate performance can be achieved for less-specular observations [56], [59], while recovering shape of specularity-dominant surfaces is still challenging. Addressing these challenges with theoretical support is one of the goals targeted by our work.

3 A MICROFACET BRDF WITH ELLIPSOID NORMAL DISTRIBUTION FUNCTION

Microfacet reflectance model postulates that surface reflectance is essentially the collective reflections with each reflection made independently by a member of a set of microfacets distributed over the surface [7], [8], [60]. Specifically, the radiance intensity can be evaluated as

$$I(\vec{v}) = \int\int_{\Omega_+} \max(\vec{m} \cdot \vec{l}, 0) D(\vec{m}) G(\vec{l}, \vec{v}) \rho_{\vec{m}}(\vec{m}, \vec{l}, \vec{v}) \, d\vec{m} \, d\vec{l}. \tag{1}$$

As illustrated in Figure 2, Ω_+ denotes the the visible upper half sphere, $\rho_m(\vec{m}, \vec{l}, \vec{v})$ evaluates the reflectance intensity contributed by a single microfacet of orientation $\vec{m}$ under
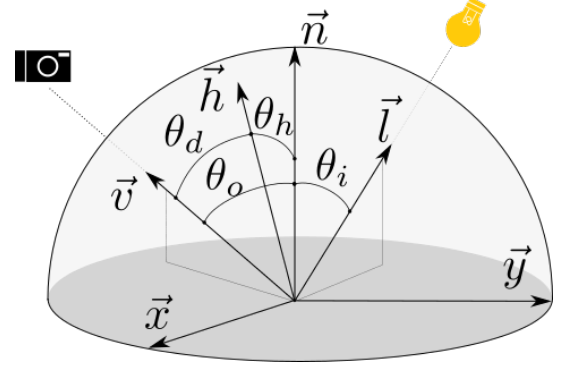

Fig. 2: The coordinates in which BRDF is defined. By convention $\vec{n} = [0, 0, 1]^\intercal$, and $\vec{v}$ and $\vec{l}$ are unit vectors that allow to orient arbitrarily above the positive half-sphere. This is in contrast to the typical setup for photometric stereo, where $\vec{v} = [0, 0, 1]^\intercal$.

directional light $\vec{l}$ when observed from $\vec{v}$, $D(\vec{m})$ is the NDF tabulating the "population" of the microfacets by their orientations, and $G(\vec{l}, \vec{v})$ is the masking-shadowing term ensuring power conservation. Because $D(\vec{m})$ and $G(\vec{l}, \vec{v})$ encode essential information about surface shape and reflectance, their geometric and algebraic properties are carefully examined in 3.1 and Section 3.2, respectively.

3.1 Ellipsoid NDF for isotropic reflectance

An ellipsoid NDF is a physically interpretable, compact and versatile representation. An important notion of the ellipsoid NDF is that, any surface is covered by a set of randomly-distributed microfacets, and these microfacets are non-overlapping and can be geometrically translated to cover the upper half of an ellipsoid seamlessly. As illustrated in Figure 3, there exits two parameterizations describing a microfacet in Ω_+: validating its point-wise location $\vec{p}$ against the ellipsoid surface function defined globally:

$$\vec{p}^\intercal S \vec{p} = 1, \tag{2}$$

or characterizing it using its own orientation $\vec{m}$ locally:

$$\vec{m} = \frac{S\vec{p}}{|S\vec{p}|}. \tag{3}$$

Here S is a 3-by-3 matrix that completely characterizes the shape of the ellipsoid and the orientation of surface normal $\vec{n}$. By enforcing the RHS of Equation 2 to be 1, we resolve the ambiguity due to arbitrary scaling. Specifically, S has following properties:

1) It is symmetric and positive definite.
2) In the case of isotropic reflectance, S denotes an ellipsoid of revolution, so its eigenvalues satisfy that $\lambda_3 \geq \lambda_2 = \lambda_1 > 0$.
3) The lengths of the major and the minor axes are $\frac{1}{\sqrt{\lambda_1}}$ and $\frac{1}{\sqrt{\lambda_3}}$ respectively.
4) The arrangement of the microfacets has to be physically consistent with the surface geometry, so the minor axis is aligned with the surface normal. Namely, $S\vec{n} = \lambda_3 \vec{n}$.
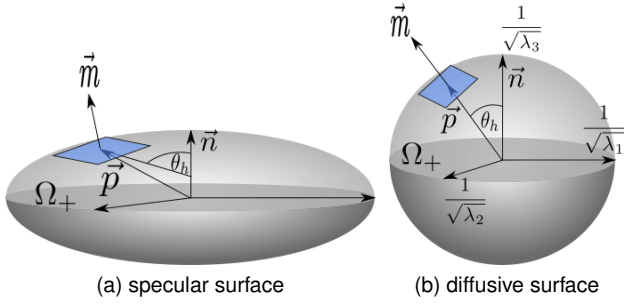
Fig. 3: The ellipsoid NDF describes that the microfacets can be re-arranged through translation to cover the upper surface of an ellipsoid. A "flatter" ellipsoid indicates that more microfacets are aligned with the surface normal $\vec{n}$, representing a smoother material.

An ellipsoid NDF is essentially a Gauss map from $\vec{m} \in \Omega_+$ to $\mathbb{R}^+$, which relies on the ellipsoidal embedding of the microfacet distribution in terms of $\vec{n}$ to associate $\vec{m}$ with a real positive value. It has been shown that defining the ellipsoid NDF as the inverse of the Gaussian curvature of the ellipsoid is both physically and algebraically viable [35]. Physically, for an ellipsoid with its Gaussian curvature decreasing at $\vec{n}$, its NDF spikes up more significantly - in its limit, all microfacets become aligned with the surface normal, and we end up with a description about mirror reflections. Algebraically, the Gaussian curvature defines the "population density" of a group of co-orienting microfacets along $\vec{m}$, which is expressed as $K_g = |S|(\vec{m}^\mathsf{T} S^{-1} \vec{m})^2$, where $|S|$ denotes the determinant of S [61]. Using Equation 2 and Equation 3, we apply spectral theorem to relate $\vec{m}$ and $\vec{n}$ explicitly. As $S = \lambda_1 \vec{u}\vec{u}^\mathsf{T} + \lambda_2 \vec{v}\vec{v}^\mathsf{T} + \lambda_3 \vec{n}\vec{n}^\mathsf{T}$, where $\vec{u}$, $\vec{v}$, and $\vec{n}$ are its eigenvectors, by definition we have $S^{-1} = \frac{1}{\lambda_1}\vec{u}\vec{u}^\mathsf{T} + \frac{1}{\lambda_2}\vec{v}\vec{v}^\mathsf{T} + \frac{1}{\lambda_3}\vec{n}\vec{n}^\mathsf{T}$. Therefore, we can express the ellipsoid NDF $D(\vec{m})$ for isotropic reflectance ($\lambda_1 = \lambda_2$) as follows:

$$D(\vec{m}) = \frac{1}{K_g} = \frac{1}{\lambda_1^2 \lambda_3 \left(\frac{(\vec{m}^\mathsf{T}\vec{u})^2 + (\vec{m}^\mathsf{T}\vec{v})^2}{\lambda_1} + \frac{(\vec{m}^\mathsf{T}\vec{n})^2}{\lambda_3} \right)^2}$$
$$= \frac{1}{\lambda_3 (1 - (\vec{m}^\mathsf{T}\vec{n})^2 + \frac{\lambda_1}{\lambda_3}(\vec{m}^\mathsf{T}\vec{n})^2)^2}. \quad (4)$$

3.2 The masking-shadowing function

As illustrated in Figure 4, the masking-shadowing function $G(\vec{l}, \vec{v})$ is introduced to impose a physical constraint under which the visible and the illuminated surface area must not exceed the projected area from either $\vec{v}$ or $\vec{l}$. When $\vec{v}$ is fixed, $G(\vec{l}, \vec{v}) = G(\theta_i)$ has to satisfy the following for isotropic reflectance [33]:

$$\vec{n}^\mathsf{T}\vec{l} = \int_{\Omega_+} \max(\vec{m} \cdot \vec{l}, 0) D(\vec{m}) G(\theta_i) \, d\vec{m}, \quad (5)$$

where $\max(\vec{m} \cdot \vec{l}, 0)$ excludes the microfacets lie in the shadow. Because typical photometric stereo assumes directional light, this highly nonlinear term only takes effect when the light significantly deviates away from the normal.
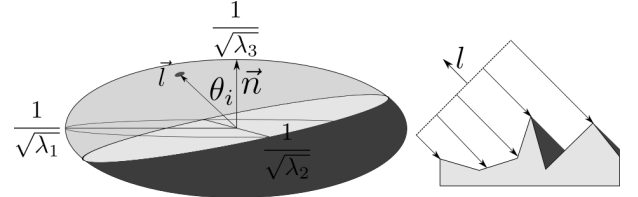

Fig. 4: The shadowing function guarantees that the total area receiving illumination over a surface of unit area does not exceed $\vec{l}^\mathsf{T}\vec{n}$. In the proposed model, the restriction that the region has to be in the upper shpere Ω_+ is removed, so the entire intersected area is considered.
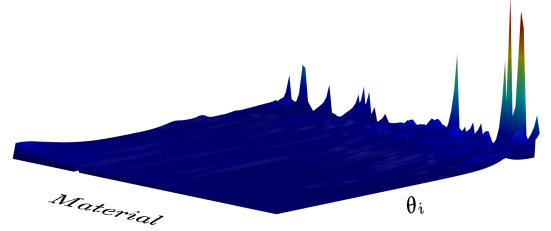

Fig. 5: A visualization of the Fresnel terms obtained in [10]. It shows that except for the grazing incident angle θ_i, each Fresnel term represents a material-specific constant.

With the premise that the object appearances are captured under the lights of sufficient distribution, it is reasonable to discard this factor from our formulation. Therefore, by plugging the widely adopted Smith Microsurface Profile [18] and the fact that $\int (\vec{h} \cdot \vec{l}) D(\vec{m}) \, d\vec{m} = \pi \sqrt{\vec{l}^\mathsf{T} S \vec{l}} |S|^{-1}$ [62] into Equation 5, we arrive at the following derivation for the shadowing function:

$$G(\vec{l}) = \frac{\vec{l}^\mathsf{T}\vec{n}}{\pi} \frac{\lambda_1 \sqrt{\lambda_3}}{\sqrt{\vec{l}^\mathsf{T} S \vec{l}}} = \frac{\vec{l}^\mathsf{T}\vec{n}}{\pi} \frac{\lambda_1 \sqrt{\lambda_3}}{\sqrt{\lambda_1(1 - (\vec{l}^\mathsf{T}\vec{n})^2) + \lambda_3(\vec{l}^\mathsf{T}\vec{n})^2}}. \quad (6)$$

3.3 The Fresnel term

In theory, the Fresnel term $F(\theta_d)$ only varies dramatically as $\theta_d \to \frac{\pi}{2}$, so in most cases it does not encode much information about shape with only exception occurs when both view and light are at the grazing angles. But this configuration rarely occurs for photometric stereo. Figure 5 visualizes the result reported in [10], in which the Fresnel term is evaluated for 100 materials in MERL BRDF Database [28]. It can be observed that, for a wide range of values chosen for θ_i (which is equivalent to θ_d in Figure 2), this term can be safely taken as an unknown constant.

3.4 A reflectance model under directional light

To model general reflectance due to directional light, each microfacet is assumed to display mirror reflection [11], namely, $\rho_m(\vec{m}, \vec{l}, \vec{v}) = F(\theta_d)\delta_{\vec{m}}(\vec{h})$ to dictate that a microfacet is "activated" to contribute to the actual reflection only when its normal $\vec{m}$ and bisector $\vec{h} = \frac{\vec{l}+\vec{v}}{|\vec{l}+\vec{v}|}$ are perfectly aligned, and according to the Fresnel equations the amount

of power it reflects is determined by the angle θ_d made by the normal and the incident light. Hence, Equation 1 can be rewritten as:

$$I(\vec{v}, \vec{l}) = D(\vec{h})G(\vec{l}, \vec{v})F(\theta_d). \qquad (7)$$

Putting Equation 1, 4 and 6 together and letting $\lambda = \frac{\lambda_1}{\lambda_3}$ leads to:

$$I(\vec{l}) = C\frac{\lambda}{(1 - (1 - \lambda)(\vec{h}^\intercal\vec{n})^2)^2}\frac{\vec{l}^\intercal\vec{n}}{\sqrt{\lambda + (1 - \lambda)(\vec{l}^\intercal\vec{n})^2}}, \qquad (8)$$

where constant C is the product of the camera gain, the Fresnel term and $\frac{1}{\pi}$. As λ defines the ratio of $\frac{1}{\sqrt{\lambda_3}}$, the length of the minor axis, to $\frac{1}{\sqrt{\lambda_1}}$, the length of the major axis, it essentially decouples the reflectance property from the absolute measurements of radiance dependent on the physical imaging process.

Algebraically, λ quantifies surface **smoothness**. Since microfacet arrangement has to be consistent with the surface geometry, we require to have $\frac{1}{\lambda_3} \leq \frac{1}{\lambda_1}$, enforcing $\lambda \in (0, 1]$. Specifically, $\lambda \to 1$ represents a sphere, $I(\vec{l}) \to C\sqrt{\lambda}\vec{l}^\intercal\vec{n}$, which describes the case of pure diffusion. This is because each microfacet is arranged along an arbitrarily selected direction of equal probability (Figure 3b). On the other hand, when $\lambda = 0$, by Equation 6 we have $G(\vec{l}) = 1$, which represents a perfectly smooth surface that displays only mirror reflection. Correspondingly, $\lambda \to 0$ represents general specular reflectance.

3.5 An approximation for specular reflectance

When $\lambda = 0$, the surface radiance represents two scenarios:

1) $\vec{h}^\intercal\vec{n} = 1$. By Equation 1, $I(\vec{l}) \to \int_{\Omega_+} D(\vec{h})\,d\vec{h} \to C\int_{\Omega_+} \delta_{\vec{n}}(\vec{h})\,d\vec{h} = C$, where $\delta(\vec{h})$ is the dirac delta function evaluated using $\frac{1}{\lambda}$.

2) $\vec{h}^\intercal\vec{n} \neq 1$. Directly from Equation 8 we have $I(\vec{l}) = \frac{C\lambda}{(1-(\vec{h}^\intercal\vec{n})^2)^2} = 0$.

In the first scenario the light is directly observed through the ideal mirror reflection, whereas in the second case no radiance is captured when the viewer moves away from $\vec{h} = \vec{n}$.

Therefore, as λ takes a sufficiently small value, and by denoting $\hat{C} = C\lambda$, we derive a reflectance function for highly specular materials:

$$I(\vec{l}) \approx \frac{\hat{C}}{(1 - (1 - \lambda)(\vec{h}^\intercal\vec{n})^2)^2}, \qquad (9)$$

which can be rearranged into

$$\sqrt{\frac{I(\vec{l})}{\hat{C}}}(1 - (\vec{h}^\intercal\vec{n})^2 + \lambda(\vec{h}^\intercal\vec{n})^2) \approx 1, \qquad (10)$$

and by isotropic symmetry that leads to $1 - (\vec{h}^\intercal\vec{n})^2 = \vec{h}^\intercal(\vec{u}\vec{u}^\intercal + \vec{v}\vec{v}^\intercal)\vec{h}$ and by spectral theorem $S = \vec{u}\vec{u}^\intercal + \vec{v}\vec{v}^\intercal + \lambda\vec{n}\vec{n}^\intercal$, Equation 10 can be further simplified as

$$((\frac{I(\vec{l})}{\hat{C}})^{\frac{1}{4}}\vec{h})^\intercal S((\frac{I(\vec{l})}{\hat{C}})^{\frac{1}{4}}\vec{h}) \approx 1. \qquad (11)$$

which is essentially the standard equation for an ellipsoid of revolution S centered at the origin. Fitting S requires at least 4 observations, a condition availed in most photometric stereo applications. An edge case arises when only mirror reflections are observed from a specific angle, but our analysis rules out this possibility as determining the orientation of a mirror surface under calibrated lighting is trivial.

4 ESTIMATING APPEARANCE AND SHAPE

Based on Equation 8, we present a unified formulation to analyze both object shape and appearance. An important notion of photometric stereo is that, the shape and reflectance properties can be inferred from the object appearance along, and presumably a better fitting to the appearance should result in a more accurate understanding about the shape and the reflectance. We follow this principle to devise our solution.

Since λ, $\vec{h}^\intercal\vec{n}$ and $\vec{l}^\intercal\vec{n}$ all lie inside $[0, 1]$, the following relations always hold:

$$1 \leq N(\lambda, \vec{n}) = \frac{1}{(1 - (1 - \lambda)(\vec{h}^\intercal\vec{n})^2)^2}, \qquad (12)$$

$$\vec{l}^\intercal\vec{n} \leq G(\lambda, \vec{n}) = \frac{\vec{l}^\intercal\vec{n}}{\sqrt{\lambda + (1 - \lambda)(\vec{l}^\intercal\vec{n})^2}} \leq 1, \qquad (13)$$

which implies that $I(\vec{l})$ is subject to a two-sided bound:

$$\hat{C}\vec{l}^\intercal\vec{n} \leq I(\vec{l}) \leq \hat{C}N(\lambda, \vec{n}). \qquad (14)$$

These two bounds bear straightforward physical significance. Since $N(\lambda, \vec{n})$ represents perfect specular reflectance and $G(\lambda, \vec{n})$ describes pure diffusion, a smoother surface always displays a stronger reflectance, but its strength is always capped by the reflectance produced by a mirror ($\lambda = 0$) under any identical lighting condition; correspondingly, radiances from an ideal diffuser ($\lambda = 1$) are constantly weaker than the actual measurement hence bounds them from below.

Equation 14 indicates that, in terms of fitting the appearances, an **optimal** estimator I_e operating with our model should perform superiorly to its counterparts that are designed with the approximations of either highly specular reflectance or the Lambert's law. Namely, $\|I_e - I\|_2 \leq \min\{\|I - \hat{C}G(\lambda, \vec{n})\|_2, \|I - \hat{C}N(\lambda, \vec{n})\|_2\}$.

4.1 A formulation for the sum of least squares

Using total K observations, we formulate a least squares problem to fit the model:

$$\min_{C, \vec{n}, \lambda} \quad \|\vec{r}(\hat{C}, \vec{n}, \lambda)\|_2^2 \qquad (15a)$$

$$\text{subject to} \quad \|\vec{n}\|_2 = 1, \vec{n}_z > 0 \qquad (15b)$$

$$1 \geq \lambda > 0, \qquad (15c)$$

$$\hat{C} > 0, \qquad (15d)$$

because estimating C and $\hat{C}$ are equivalent. Here $\vec{r}$ is a vector of K entries. Its k-th entry, $r_k = I_e(\vec{l}_k) - I_k$, represents the estimation error evaluated at $I_e(\vec{l}_k) = \hat{C}N_kG_k$

in terms of $\vec{n}$ and λ for light $\vec{l_k}$. The solution satisfies the necessary first-order optimality condition: $\nabla \vec{r}^\intercal \vec{r} = 0$. For each measurement the gradient $\nabla \vec{r}_k$ can be further decomposed as $\nabla(\hat{C} N_k G_k) = \hat{C} G_k J_{N,k} + \hat{C} N_k J_{N,k}$, where $J_{N,k}$ and $J_{G,k}$ are the rows of K-by-4 Jacobian matrices J_N and J_G that are derived with respect to $N(\lambda, \vec{n})$ and $G(\lambda, \vec{n})$. Also, we denote D_N and D_G as two K-by-K diagonal matrices whose k-th diagonal entry represents N_k and G_k, respectively. Since $\hat{C}$ can be evaluated in a separate step in locating the stationary points, an optimal solution $\vec{x}^* = [\vec{n}^*, \lambda^*]$ should necessarily satisfy that

$$\vec{r}^\intercal(\vec{x}^*) J = \vec{r}(\vec{x}^*)^\intercal (D_G J_N + D_N J_G) = 0. \quad (16)$$

This general formulation subsumes multiple special instances defined over a more restrictive solution space. When $\vec{n}$ is provided, estimating surface smoothness λ amounts to reflectance analysis; when λ is assigned to be 0, solving $\vec{n}$ dedicates to shape estimation for specular surfaces; in addition, if we enforce $N(\vec{n}, \lambda)$ to be 1, the resulting formulation enables the classic shape recovery for Lambertian surfaces. These subproblems are addressed using the sub-matrices of the Jacobian matrices J_N and J_G constructed as follows:

$$\frac{\partial N_k}{\partial \lambda} = -2\big(1 - (1-\lambda)(\vec{h}_k^\intercal \vec{n})^2\big)^{-3}(\vec{h}_k^\intercal \vec{n})^2 \le 0, \quad (17)$$

$$\frac{\partial G_k}{\partial \lambda} = -\frac{1}{2}\big(1 - (\vec{l}^\intercal \vec{n})^2\big)\big(\lambda + (1-\lambda)(\vec{l}^\intercal \vec{n})^2\big)^{-\frac{3}{2}} \le 0, \quad (18)$$

$$\frac{\partial N_k}{\partial \vec{n}} = 4\big(1 - (1-\lambda)(\vec{h}^\intercal \vec{n})^2\big)^{-3}(\vec{h}^\intercal \vec{n})(1-\lambda)\vec{h}, \quad (19)$$

$$\frac{\partial G_k}{\partial \vec{n}} = \big(\lambda + (1-\lambda)(\vec{l}^\intercal \vec{n})^2\big)^{-\frac{3}{2}} \lambda \vec{l}. \quad (20)$$

4.2 Estimating surface smoothness

It is not hard to verify that $\|\vec{r}\|_2$ with respect to λ is a single-variable non-convex function, and by Equation 17 and 18, $\frac{\partial r_k}{\partial \lambda}$ is constantly negative. Monotonicity and Equation 14 suggest that we can apply λ being initialized from both ends of its domain: $\lambda_0 = 1$ and $\lambda_0 = 0$ to a nonlinear least square solver. Accordingly, the solution for λ and $\hat{C}$ always satisfies the following:

$$\|\vec{r}(\lambda^*, C^*)\|_2 \le \min\{\min_{\lambda, \hat{C}} \sum_k \|\hat{C} N_k - I_k\|_2,$$
$$\min_{\lambda, \hat{C}} \sum_k \|\hat{C} \vec{l}_k^\intercal \vec{n} - I_k\|_2\}, \quad (21)$$

with the equality holds when the surface happens to be highly specular or ideally diffusive.

Illumination **coverage** is critical to determining λ. In theory, two observations are sufficient to define a well-posed problem. However, in practice, insufficient coverage of lighting leads to numerical ambiguities. For instance, when $\vec{h}^\intercal \vec{n} \ll 1$, we also have $\vec{l}^\intercal \vec{n} \ll 1$ due to geometrical constraint, which leads to $N(\sqrt{\lambda}) \to \lambda$ and $G(\sqrt{\lambda}) \to \sqrt{\lambda}$. Furthermore, Equation 8 can be reduced as

$$I(\vec{l}) = C\sqrt{\lambda} \vec{l}^\intercal \vec{n}, \quad (22)$$

which also represents the Lambert's cosine law. This indicates that, if the specularity is not captured (e.g. no $\vec{h}_k$ is well-aligned with $\vec{n}$ during sampling), an actually highly specular surface with $\lambda \to 0$ might be misperceived to be a diffusive surface with $\lambda \to 1$, whereas $\vec{n}$ is invariant. This fact essentially justifies the step of pre-filtering adopted in [43], [45], [58], where specularities are deliberately eliminated for only estimating the surface shape. However, when it comes to determining the reflectance property, we should not dismiss the observations of specular reflectance. Section 5.2.2 demonstrates this case experimentally.

4.3 Estimating surface normal

When $\vec{n}$ is treated as a variable, the corresponding Jacobian matrix behave similarly to Equation 8. Specifically, when $\lambda \to 1$, $J \to J_G$, and when $\lambda \to 0$, $J \to J_N$. The former describes a convex problem so it is easy to solve; the optimal solution to the latter can also be obtained using the method introduced in [13], which can also be explained in a coherent formulation with Equation 16 as illustrated in Section 4.3.1. Subsequently, in Section 4.3.3 we show that these solutions arising from both simplifications can be effectively extended to addressing the problem of general reflectance.

4.3.1 Normal estimation with $\lambda \to 0$

As derived in Section 3.5, estimating the normal of a highly specular surface boils down to fitting an unknown ellipsoid of revolution in $\mathbb{R}^3$ using re-scaled $\vec{h}$ by $\left(\frac{I(\vec{l})}{\hat{C}}\right)^{\frac{1}{4}}$. We show that fitting an ellipsoid amounts to minimizing a sum of squares defined by Equation 15a, and its solution lies in a set of solutions to a system of polynomials in the form of Equation 16.

To get around the unit norm constraint on $\vec{n}$, one can also let $\hat{n} = \sqrt{\frac{(1-\lambda)}{\hat{C}}} \vec{n}$, hence for each of the K observations, Equation 10 can be rewritten as

$$\sqrt{I(\vec{l}_k)} \left(\sqrt{\frac{1}{\hat{C}}} - \hat{n}^\intercal \vec{h}_k \vec{h}_k^\intercal \hat{n} \right) = 1, k = 1, 2, \cdots, K, \quad (23)$$

and by averaging all K equations, we obtain $\bar{I} = \frac{1}{K} \sum_{k=1}^{K} \sqrt{I(\vec{l}_k)}$, $\bar{H} = \frac{1}{K} \sum_{i=1}^{K} \sqrt{I(\vec{l}_k)} \vec{h}_k \vec{h}_k^\intercal$, and

$$\sqrt{\frac{1}{\hat{C}}} = \frac{1 + \hat{n}^\intercal \bar{H} \hat{n}}{\bar{I}}, \quad (24)$$

Moreover, substituting $\sqrt{\frac{1}{\hat{C}}}$ in Equation 23 with Equation 24 leads to

$$\hat{n}^\intercal \left(\sqrt{I(\vec{l}_k)} \vec{h}_k \vec{h}_k^\intercal - \sqrt{I(\vec{l}_k)} \frac{\bar{H}}{\bar{I}} \right) \hat{n} = \frac{\sqrt{I(\vec{l}_k)}}{\bar{I}} - 1, \quad (25)$$

a quadratic polynomial of three variables in terms of $\hat{n} = [\hat{n}_1, \hat{n}_2, \hat{n}_3]^\intercal$. Therefore, all K equations in the form of Equation 25 can be organized into the matrix form

$$Mx(\hat{n}) = M[\hat{n}_1^2, \hat{n}_1 \hat{n}_2, \hat{n}_1 \hat{n}_3, \hat{n}_2^2, \hat{n}_2 \hat{n}_3, \hat{n}_3^2]^\intercal = b, \quad (26)$$

where $M \in \mathbb{R}^{K \times 6}$ and $b \in \mathbb{R}^K$.

The solution to Equation 26, $\hat{n}^*$, relates to the minimizer $\vec{n}_s$ for the sum of squares

$$\|r(\vec{n})\|_2^2 = \|Mx(\hat{n}) - b\|_2^2 = x^\intercal M^\intercal M x - 2b^\intercal M x + b^\intercal b, \tag{27}$$

in that $\frac{\hat{n}^*}{\|\hat{n}^*\|_2} = \vec{n}_s$. Since the cost function in Equation 27 is nonconvex, we need to minimize it by examining all its stationary points. Specifically, it is feasible to solve the three-variable cubic equations defined by the partial derivatives as

$$\frac{\partial \|r(\hat{n})\|_2^2}{\hat{n}_1} = 0, \frac{\partial \|r(\hat{n})\|_2^2}{\hat{n}_2} = 0, \frac{\partial \|r(\hat{n})\|_2^2}{\hat{n}_3} = 0. \tag{28}$$

which is a three-variable cubic polynomial system that has 27 solutions. Since the system is homogeneous, the solutions are positive-negative symmetric. Therefore, we only need to examine 13 independent solutions. These facts motivate a solver based on the symmetric Gröbner basis [63]. The resulting $\hat{n}$ is optimal, so does $\vec{n}_s$ yield an optimal solution to Equation 16 for $\lambda \to 0$:

$$r(\vec{n}_s)^\intercal J_N = 0, \tag{29}$$

based on which $\hat{C}_s$ is obtained subsequently.

4.3.2 Normal estimation with specified $\lambda \in (0, 1]$

Let $\{\vec{n}_d, \hat{C}_d\}$ denote the optimal solution to the convex problem defined when $\lambda \to 1$. Necessarily, it has to satisfy

$$r(\vec{n}_d)^\intercal J_G = 0. \tag{30}$$

We show that, either $\{\vec{n}_d, \hat{C}_d\}$ or $\{\vec{n}_s, \hat{C}_s\}$ serves as a good initial input for problem 15a, which is to obtain the orientation of a surface with general and known reflectance. Our discussion focuses on the structure of our model that facilitates its effective integration with the standard nonlinear least-squared solver. In particular, Equation 19 and 20 indicate that asymptotically

$$J^\intercal J \approx D_G^2 J_N^\intercal J_N + D_N^2 J_G^\intercal J_G \tag{31}$$

because the cross-terms in the product vanish in the vicinity of $\lambda \to 0$ and $\lambda \to 1$. It is also readily seen that $J^\intercal J$ is a 3-by-3 positive-definite matrix because both D_N and D_G have positive diagonal entries.

We still aim to solve Equation 16, but instead of solving it directly, we need an initial input $\vec{n}_0$, from which an updating vector $\vec{p}_n$ satisfying $\nabla \vec{r}^\intercal \vec{p} < 0$ is determined so that $\|\vec{r}(\vec{n}_0 + \vec{p})\|_2 \leq \|r(\vec{n}_0)\|_2$. Apparently by Equation 29 and 30 both $\vec{n}_s$ and $\vec{n}_d$ satisfy this condition. Since a non-linear least square solver operates accurately in an open neighborhood of $\vec{n}_0$ where $\vec{r}(\vec{n}) = \vec{r}(\vec{n}_0) + J(\vec{n}_0)^\intercal (\vec{n} - \vec{n}_0)$ consistently holds, it is expected to reach a local minimum in this neighborhood if Equation 31 is also valid.

Although we assign $\vec{n}_0$ to be either $\vec{n}_s$ or $\vec{n}_d$, through iterations $\vec{n}$ updates, so the resulting local optima may deviate far from the initial input. After all, achieving a matrix that is consistently positive-definite by Equation 31 is a much more relaxed condition than simply enforcing $\lambda \to 0$ or $\lambda \to 1$. It is worth noting that our analysis connects with the formulation of piece-wise smoothness described in [45], as in both cases the second order derivative $\|\nabla^2 \vec{r}\|_2$ is considered to be negligibly small. Nevertheless, our solution is more general as it also covers specular reflectance.

4.3.3 Normal estimation with unknown $\lambda \in (0, 1]$

Putting it altogether, our solution to photometric stereo with general isotropic reflectance operates as follows:

Step 1 Obtain the optimal solution, $\{\vec{n}_s, \hat{C}_s\}$, that minimizes problem 15a with $\lambda = 0$ using the polynomial solver introduced in Section 4.3.1.

Step 2 Obtain the optimal solution, $\{\vec{n}_d, \hat{C}_d, \lambda_d\}$, that minimizes problem 15a with $\lambda = 1$.

Step 3 Initialize $\vec{x}_0 = \{\vec{n}_0, \hat{C}_0, \lambda_0\}$ with $\{\vec{n}_s, \hat{C}_s, 0\}$ and $\{\vec{n}_s, \hat{C}_s, \lambda_d\}$ in two separate executions, then feed them to the least square estimator for problem 15a.

Step 4 Select λ^*, C^* and $\vec{n}^*$ that minimizes $\|\vec{r}\|_2$ between the two candidate solutions.

Again, in two scenarios the pixel-wise estimation for λ may conclude the surface to be diffusive: the surface is intrinsically diffusive or a specular surface is perceived to be diffusive due to insufficient sampling. In either case $\hat{C} = C\lambda$ cannot be resolved due to light-albedo ambiguity, but this does not affect our estimation for $\vec{n}$. Moreover, since our model addresses strong specularities directly rather than treating them as outliers, the step for pre-prefiltering [58] becomes optional but preserving it in our procedure does not introduce counter effect. Finally, we expect our minimizer to satisfy the following:

$$\|\vec{r}(\lambda^*, C^*, \vec{n}^*)\|_2 \leq \min\{\|\vec{r}(\lambda = 1, \hat{C}_d, \vec{n}_d)\|_2, \\ \|\vec{r}(\lambda = 0, \hat{C}_s, \vec{n}_s)\|_2\}. \tag{32}$$

5 EXPERIMENT

We use both synthesized and real images to validate our proposed model and to evaluate our algorithm. Since shadowing and inter-reflections are not considered, we use PBRT [64] and the MERL BRDF [28] of 100 materials to synthesize various appearances of a sphere under six different distributions of directional lights, as illustrated in Figure 6. In addition to generating a set of uniformly-distributed light directions from the spiral points over a unit sphere [65] (Figure 6a, 6b, 6c, 6d), we also consider adverse lighting conditions such as non-uniform distribution (Figure 6e) and partial coverage (Figure 6f). Throughout our experiments, we assume the inputs are captured from an orthographic camera with linear response. Moreover, we use DiLiGent [58] dataset to benchmark the performance of our estimator on real scenes. Unless otherwise stated, in our setup all methods take the raw input **as is**, namely all non-zero pixel values are considered for evaluation.

5.1 Model validation

We apply two types of metric to validate our reflectance model: we first examine if the surface smoothness λ obtained according to Section 4.2 is consistent with our subjective perception about the materials; concomitantly, we also evaluate the error resulted from directly fitting the object appearance.

(a) 60 lights   (b) 150 lights   (c) 250 lights
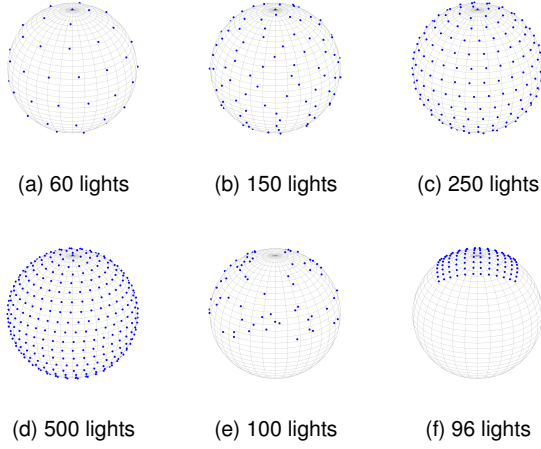
(d) 500 lights   (e) 100 lights   (f) 96 lights

Fig. 6: Distribution of lights with various densities and patterns. The view vector $v = (0, 0, 1)$ is pointing upward. Hence the lights located in the bottom are expected to contribute less to appearance formation.

methods	500	250	150	60	100	96
ours	2.16	2.33	2.48	3.07	2.48	4.80
VE [66]	0.59	0.63	0.69	0.80	1.10	2.21
Bi-Quad [59]	18.31	17.70	16.86	15.83	10.72	8.78
CBR [56]	4.54	4.58	4.07	6.11	3.23	7.19
Torrence	14.68	14.92	14.95	14.88	15.36	13.20
Ward	2.81	3.13	3.74	4.76	8.74	13.06

TABLE 1: Comparison of the mean estimation error in degrees of surface normal of 100 spheres under all six illumination conditions. *VE* is trained using all 100 materials, and no pre-filtering is performed on the inputs.

5.1.1 Estimation for surface smoothness

Sharing an identical set of lightings, surfaces of different orientations are unevenly-sampled. As a result, we inevitably end up with inconsistent estimation of λ across pixels even though they represent a single material. In this case, we employ a heuristic that picks the pixel displaying the most effective measurements (in L2 norm) to deliver a reliable estimation. Figure 7 plots the estimated λ under all six illumination conditions using the approach described in Section 4.2. The materials are sorted according to λ estimated under 500 lights. As expected, the ranking of materials by λ is consistent with our perception about the material smoothness.

It is worth noting that, in the cases of estimation inconsistencies, for each material the most densely and uniformly distributed samples always produce the smallest estimation for λ. This is because this setting offers the highest chance to capture the complete occurrences of specularities. After all, a highly localized specularity is a prominent cue for material perception, but it is also one of the hardest to be detected by directional light. Also, when the material is purely diffusive, the way it is being perceived is not sensitive to the lighting anymore, hence all traces meet at right end of Figure 7.

5.1.2 Fitting object appearance

Figure 8 compares the performance of our proposed model and the performances of other representative reflectance models (Cook-Torrence, Lafortune, Ward and Biquadratic (*Bi-Quad*) [59]) on fitting the appearance of a sphere.[1] The normalized mean squared fitting error is evaluated and averaged over all pixels so that all models can be compared using a unified metric. As described in Section 4.2, appearance analysis desires for dense sampling, the performances of all models are compared under 500 lights. Overall speaking, our model outputs a stable and accurate estimation for object appearances for all 100 materials.

---

1. We show a per-normal representation of BRDF fitting results in the supplementary material.

Specifically, one can observe that our model outperforms most other models more significantly on fitting specular appearances. This evidences the fact that our model can predict the spatial variation of specularities accurately. Reasonably, other models (e.g. Ward) may achieve a better result on some materials at an increased complexity, however, as to be presented in Section 5.2, complex models unavoidably invite instabilities in surface normal estimation.

5.2 Photometric stereo on synthesized scenes

Figure 9 compares the angular error in degrees produced by the estimations made by our method, Torrance, Ward, *Bi-Quad*, Constrained Bivariate Regression (*CBR*) [56] and Virtual Exemplars (*VE*) [66] when applied to photometric stereo under 500 lights (Figure 6d). To the best of our knowledge *Bi-Quad* and *CBR* are the state-of-the art models, and *VE* is completely data driven. We train the *VE* under each light distribution using all 100 MERL materials, which is its optimal setup in our experiment.

The average estimation error over all six light distribution is also summarized in Table 1. It can also be observed that, our model accurately recovers the surface normal and is the least susceptible to illumination variation compared with all other models. It is worth noting that Ward performs inferiorly as light distribution becomes sparser. Also, because *VE* is trained and tested on the same data set so its inputs are utterly represented, expectedly it outperforms other model-based approaches. According to Table 1, the general performance gap between our method and *VE* is between 1.3 degrees (under 100 lights) and 2.6 degrees (under 96 lights), which is on average 2 degrees narrower compared with the second best model-produced result by *CBR*.

Additionally, Figure 10 compares the performance of our estimator under all six illumination distributions. As expected, denser samples produce less estimation error, but our method is resilient to illumination variation as the corresponding precision fluctuation is marginal.

5.2.1 Performance bound

In Section 4.3 we expect that $\{\hat{C}^*, \lambda^*, \vec{n}^*\}$ should be more accurate than both $\{\lambda = 0, \hat{C}_s, \vec{n}_s\}$ and $\{\lambda = 1, \hat{C}_d, \vec{n}_d\}$. Plots in Figure 11 empirically endorse our expectation. Specifically, we observe that most specular materials are well addressed by our specular solver, and its error trace is exactly complementary (with only one intersection) to the error trace produced by the least square solver. More importantly, our iterative approach targeting on general
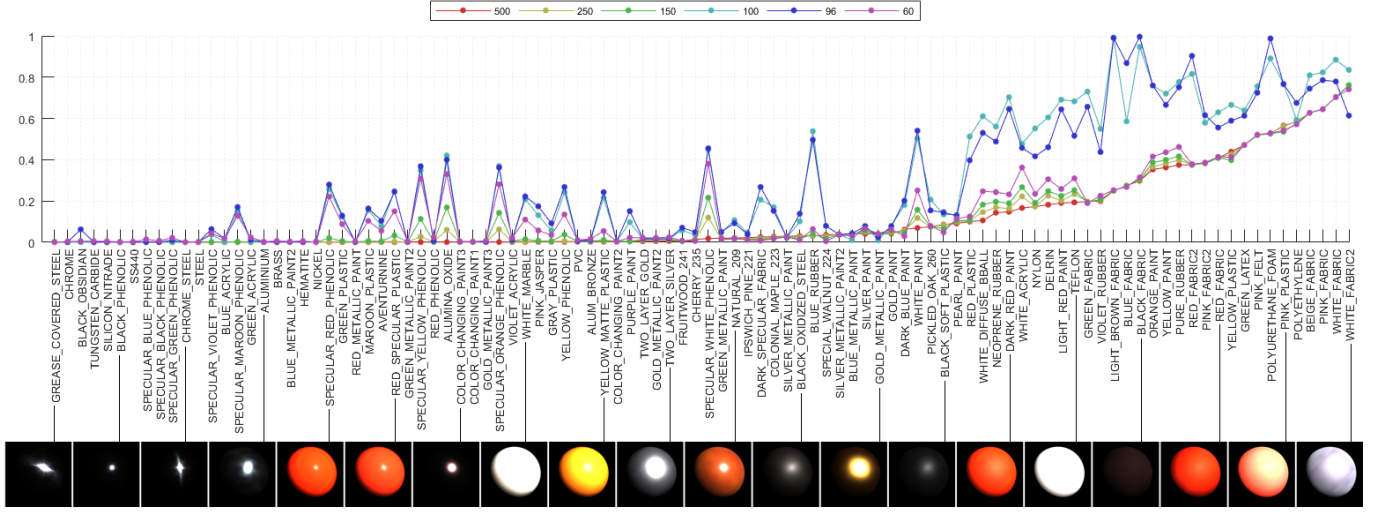
Fig. 7: Estimation of surface smoothness for 100 MERL materials using the appearances of the corresponding sphere. The materials are ranked according to the respective estimated value for λ. The ranking is consistent with the perception of the surface smoothness. Also, the denser the light, the more likely a material is deemed specular because specularities have higher chance of being observed.
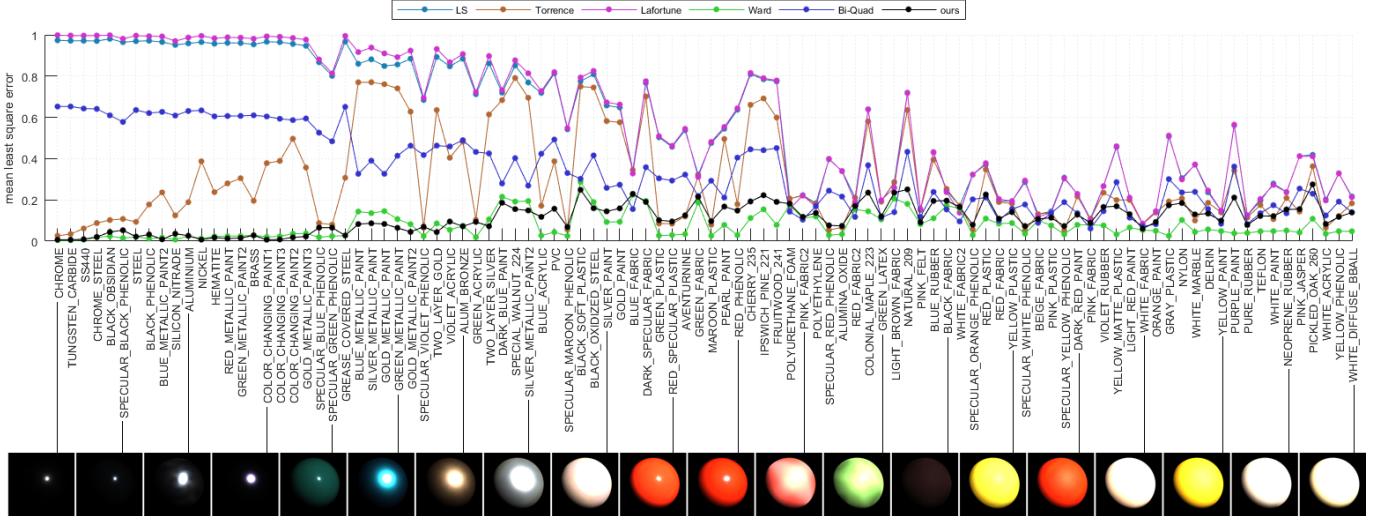

Fig. 8: Normalized appearance fitting error of spheres synthesized using 100 MERL materials.

reflectance performs much better than both solvers across all 100 materials, directly validating our formulation in Equation 8 and our discussion in Section 4.3.2.

5.2.2 Ambiguous interpretation about surface smoothness

Section 4.2 derives the fact that specular surfaces have a chance of being correctly recovered even the specularities they display are not captured. Figure 12 presents an empirical evidence using our estimations for "PVC". We observe that the estimation error produced by $\{\vec{n}_s, \hat{C}_s\}$ (Figure 12a) and that produced by $\{\vec{n}_d, \hat{C}_d\}$ (Figure 12b) also exhibit a pair of complementary patterns spatially. Although $\{\vec{n}^*, \hat{C}^*\}$ produces a better estimation (Figure 12c), the per-pixel interpretations about smoothness, λ^*, are inconsistent: surface points in the brighter regions orient away from the observer, forming a geometric constraint due to which specularities are less likely to observe from them. As a result, they are perceived to be highly diffusive even

though their shape is correctly interpreted (12d). Again, this fact justifies the approaches that pre-filter specularities as outliers for shape recovery, despite that they often misjudge the reflectance properties.

5.3 Photometric stereo on real scenes

Table 2 compares the estimation error in degrees obtained using the proposed approach with the error resulted by other approaches.[2] Multiple pre-filtering strategies discussed in [58] are applied to optimize the results. For our model, we simply discard the shadowed pixels as their readings are insignificant. This table is divided into two charts: the upper chart compares the scores obtained the model-based approaches, where the performance gain achieved by our model is obvious. In particular, more significant

2. The visualizations of the estimated surface normals are presented in the supplementary material.
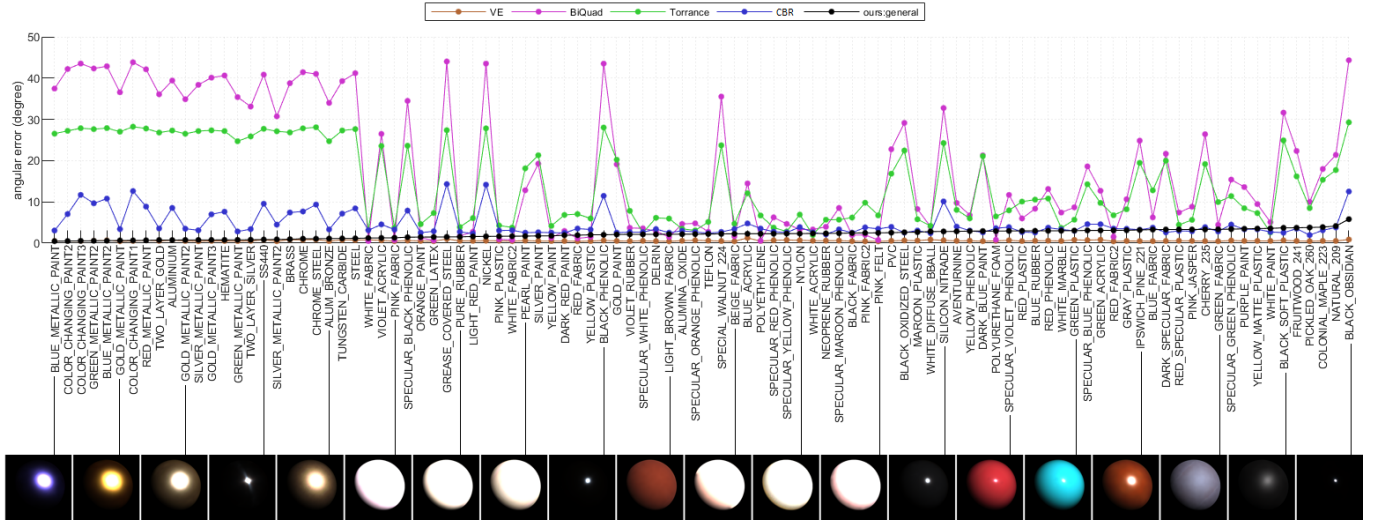
Fig. 9: Angular error in degrees of shape estimation for spheres made of 100 MERL materials. *VE* is trained using all 100 MERL materials. Our methods deliver comparative results, especially over the specular surfaces.
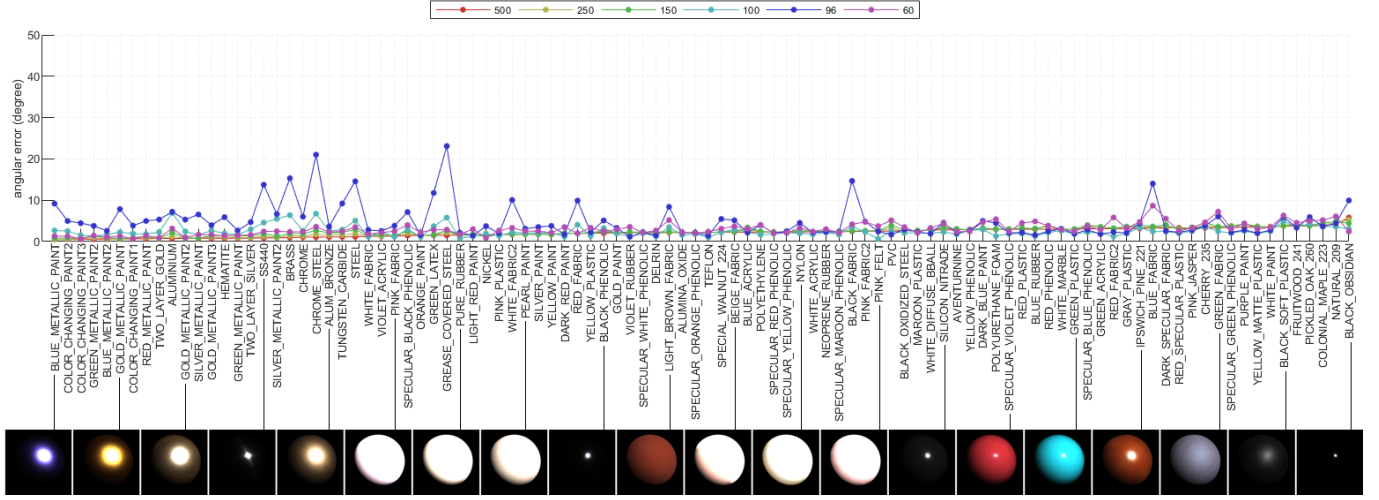

Fig. 10: Angular error in degrees of shape estimation under various lightings. The denser and more complete the light distribution is, the better the performance is to be achieved. Besides, our proposed approach is resilient to illumination distribution.
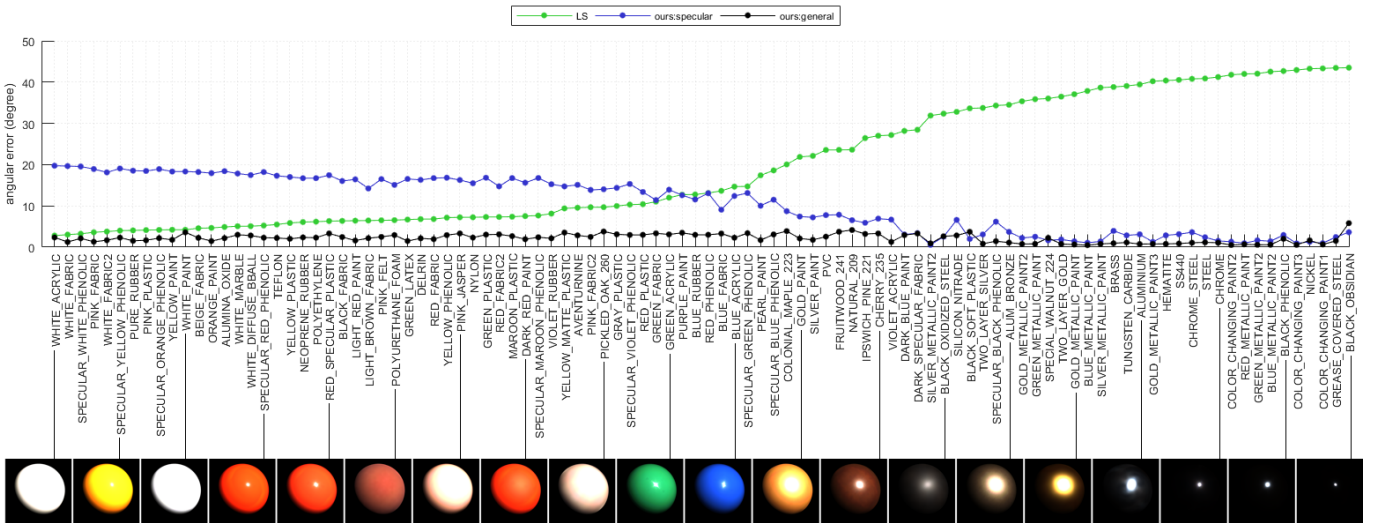

Fig. 11: Empirical evidence for the existence of the bound on the worst case performance. Namely, the iterative solver in theory should always produce better results than the solver assuming purely diffusion ($\lambda = 1$) and purely specular ($\lambda = 0$).

methods		ball	cat	pot1	bear	pot2	buddha	goblet	reading	cow	harvest	average
WG10 [43]	mean	2.03	6.72	7.18	6.50	13.12	10.91	15.70	15.39	25.89	30.00	20.47
	median	2.11	5.70	5.64	4.88	8.92	8.51	12.34	9.70	26.81	24.08	10.87
IW12 [44]	mean	2.54	7.21	7.74	7.32	14.09	11.11	16.25	16.16	25.70	29.26	13.74
	median	2.29	6.02	6.09	5.88	10.58	8.73	13.27	9.37	26.50	16.11	10.48
GC10 [3]	mean	3.21	8.22	8.53	6.62	7.90	14.85	14.22	19.07	9.55	27.84	12.00
	median	1.17	4.67	4.01	3.61	3.37	7.57	8.01	14.07	5.79	20.22	7.25
AZ08 [54]	mean	2.71	6.53	7.23	5.96	11.03	12.54	13.93	14.17	21.48	30.51	12.61
	median	2.47	4.32	4.70	3.97	8.40	7.62	9.64	7.23	21.52	18.34	8.82
HM10 [51]	mean	3.55	8.40	10.85	11.48	16.37	13.05	14.89	16.82	14.95	21.79	13. 22
	median	2.86	6.07	7.35	9.81	13.07	9.14	10.10	11.34	12.70	14.88	9.73
ST12 [67]	mean	13.58	12.33	10.37	19.44	9.84	18.37	17.80	17.17	7.62	19.30	14.58
	median	12.32	9.57	7.52	19.07	6.67	15.48	14.04	12.74	3.91	13.58	11.49
ST14 [59] (Bi-Quad)	mean	1.74	6.12	6.51	6.12	8.78	10.60	10.09	13.63	13.93	25.44	10.30
	median	1.57	4.04	4.05	4.38	6.50	6.89	7.27	7.59	12.17	17.12	7.16
IA14 [56] (CBR)	mean	3.34	6.74	6.64	7.11	8.77	10.47	9.71	14.19	13.05	25.95	10.60
	median	3.33	4.86	4.24	5.57	6.57	6.71	6.59	8.21	10.59	17.40	7.41
ours	mean	1.98	5.47	6.11	5.54	7.15	9.82	9.68	16.82	7.47	19.03	8.91
	median	1.78	3.33	3.14	3.25	4.35	6.41	7.30	7.54	4.10	9.44	5.06
HS17 [66] (VE)	mean	1.33	4.88	5.16	5.58	6.44	8.48	7.57	12.08	8.23	15.81	7.56
	median	0.91	3.04	2.55	4.45	3.18	5.36	5.10	5.35	4.58	7.74	4.23
SS17 [4]	mean	2.02	6.54	7.05	6.31	7.86	12.68	11.28	15.51	8.01	16.86	9.41
	median	1.14	3.43	3.39	3.67	4.13	6.92	6.04	7.61	4.49	9.05	4.99
TM18 [57]	mean	1.47	5.44	6.09	5.79	7.76	10.36	11.47	11.03	6.32	22.59	8.83
	median	1.26	3.87	3.46	4.38	5.57	7.38	9.47	7.33	4.41	19.90	6.70
PS-FCN [6]	mean	2.26	5.47	6.11	9.42	7.15	10.24	9.68	16.82	7.48	19.03	9.36
	median	1.99	3.37	3.14	5.42	4.36	6.21	7.30	7.55	4.11	9.44	5.29

TABLE 2: Comparison of mean and median of estimation error with the benchmark results [58]. It can be observed that our results outperform all the estimations made by other models listed in the upper table, and they are also comparable to the estimations obtained using recent data-driven methods listed in the lower table.
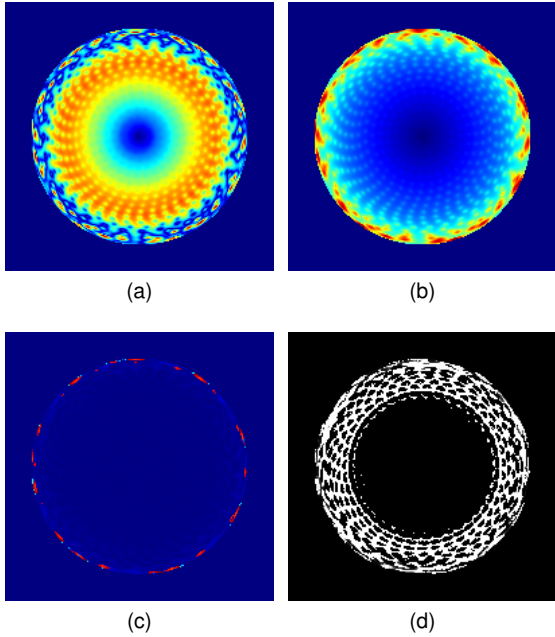

Fig. 12: Ambiguous interpretation about surface smoothness arises even when surface shape is correctly estimated: (a) per-pixel estimation error resulted from $\vec{n}_d$ and $\lambda = 1$; (b) error resulted from $\vec{n}_s$ and $\lambda = 0$; (c) error resulted from $\vec{n}^*$ and λ^* obtained by the iterative solver; (d) the per-pixel estimation of λ^*. The dark region represents surfaces deemed specular, and the bright represents surfaces deemed diffusive. $\lambda \in (0, 1]$.

performance gain is achieved over surfaces with complex reflectance (e.g. "cow" and "harvest"); Lower chart lists the state-of-the-art results obtained using the data-driven approaches. Overall speaking, *VE* delivers most satisfactory results, while in comparison, our method performs inferiorly over "reading" and "harvest" due to the presence of inter-reflections and cast shadows. Undeniably, this indicates a common advantage of data-driven approaches over their model-based counterparts.

Table 3 reports the benchmark results obtained without pre-filtering, namely, all non-zero readings are considered. We see that, our method is resilient to pre-filtering, since the estimations are close to the numbers reported in Table 2. In particular, we make two observations: First, the performance gap reduces over complex reflectance (e.g. "reading","cow" and "harvest"), while in contrast *Bi-Quad* and *CBR* are susceptible to specularities. Second, our result draws strong parallelism with *VE*, which evidences that our model completely captures the physical nature of reflectance measurements. In particular, both methods exhibit a gap of 1.6 degrees , indicating that the performance gap between our method and *VE* (approximately 1.5 degrees) is consistent and stable. As discussed in Section 5.4, this minor performance gain is achieved at an extra cost of significant amount of computation and storage.

5.3.1 Simultaneous shape and reflectance acquisition

We also apply our method on the "helmet" from the "Light Stage Data Gallery" [68], and transfer its reflectance to "Buddha" to produce its relit appearances as exemplified in Figure 13. We can observe that the correct shape of the helmet is obtained, and the specular feature of its surface is also properly ported to a different model. In contrast to direct appearance-to-appearance transfer, this process

methods		ball	cat	pot1	bear	pot2	buddha	goblet	reading	cow	harvest	average
ST14 [59] (Bi-Quad)	mean	5.09	9.28	9.93	9.37	15.25	16.58	18.12	21.09	21.34	30.22	15.63
	median	2.59	7.12	7.43	6.68	12.94	11.75	15.81	14.68	20.38	24.27	12.37
IA14 [56] (CBR)	mean	9.36	9.89	10.40	10.66	10.57	15.95	15.23	19.94	17.70	28.66	14.84
	median	7.08	7.08	7.11	6.87	7.16	9.33	9.62	13.53	17.28	24.44	10.95
ours	mean	3.61	7.08	7.30	10.36	7.95	12.74	11.50	17.14	8.21	20.03	10.60
	median	2.04	3.88	3.82	6.33	4.72	7.48	7.87	8.36	4.19	10.32	5.91
HS17 [66] (VE)	mean	1.50	6.17	6.70	6.88	6.61	12.93	10.50	14.38	8.42	17.53	9.17
	median	1.02	3.13	2.90	4.56	3.44	6.57	5.53	6.31	4.71	8.51	4.67

TABLE 3: Comparison of mean and median of estimation error with some state-of-the-art benchmark results [58] without illumination filtering. It can be observed that our result is also resilient to illumination filtering. This evidence of stability becomes more obvious when our method is applied to complex appearances (e.g. "cow", "reading" and "harvest").
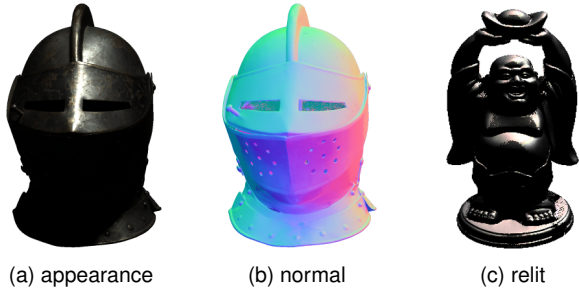

Fig. 13: An example of simultaneous physical interpretation of shape and surface reflectance: our method is first applied to (a) appearances in order to obtain the corresponding (b) normal map and λ for each channel. Then we apply λ to our estimated normal map of "Buddha" using Equation 8. This is a physics-driven process as it does not directly transform the reflectance from one appearance to another.
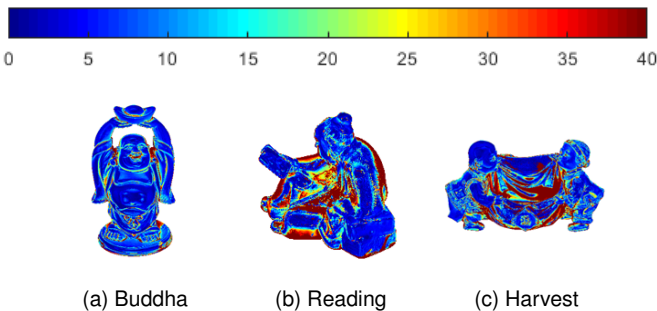

Fig. 14: Angular error maps (degree) produced by our model applying to the DiLiGent data set [58]. Cast shadows and inter-reflctions due to non-convex shape are the main sources of our estimation error. These phenomena are inherently not addressed by stand-alone models for surface reflectance.

acquires shape and reflectance before integrating them for relighting, so it necessitates accurate physical interpretation as opposed to algebraic transformations.

5.4 Comparison with data-driven approaches

Although our empirical results indicate that the state-of-the-art data-driven approaches achieve higher accuracies comparing to our model-based solution, they do not endorse the view that reflectance models are obsolete. On contrary, the superiority of our approach is obvious. First,

in runtime, our solver is extremely light weight that it leaves almost no memory footprint. Namely, in contrast to the five parameters (C, λ, $\vec{n}$) estimated by our solver, deep learning applications are incommensurably intensive in both computation and memory usage. Even compared with *VE*, our solver achieves approximately 15 times speed-up in efficiency in a single thread environment (our solver processes the DiLiGent data set at the rate of 0.019 seconds per pixel). Second, data-driven methods necessitate heavy duty training. For example, *VE* has to populate 5GB offline dictionary for only 96 lights, and the size of the training data used by the deep neural net in [4] is 4.5GB. More importantly, this significant amount of training data is largely illumination-dependent, which is a major reason that prevents them from flexible deployment. In comparison, our solution is plug and play.

Admittedly, despite the versatility and accuracy of our model, in general, data-driven approaches have displayed promising potential in modeling and analyzing complex object appearances. After all, the design of reflectance models is only intended for scenes without interreflections and cast shadows, as illustrated in Figure 14. However, as the results of "reading" and "harvest" in Table 2 suggest, state-of-the-art data-driven methods that directly leverage training samples for end-to-end inverse mapping have not yet converted this potential to their actual advantage. Therefore, we foresee that a potential cure may be an interpretable and invertible generative model that can successfully disentangle shape, material and illumination. To this end, our proposed model can serve as a useful building block.

6 CONCLUSION

This paper presents a versatile and invertible microfacet-based reflectance model to address photometric stereo over surfaces displaying isotropic reflectance. Its relative worst case performance is bounded both theoretically and experimentally. Our experiments also firmly demonstrate that the proposed model outperforms other models in most cases of illumination distribution and surface reflectance, and it even delivers comparable performance in accuracy with the state-of-the-art data-driven approach but is much more light-weight, flexible and efficient. In the standard setup for photometric stereo where directional light is used, it serves as an off-the-shelf solution.

Through our experiment we have also witnessed the common limitation of model-based approach in analyzing complex object appearances such as cast shadows and inter-reflections. Comparatively, the state-of-the-art data-driven

implementations are end-to-end and trade excessive flexibility, efficiency and storage for a relatively marginal improvement. Since our model is proved successful in reflectance analysis, we argue that resources can be further optimized towards solving the intrinsically difficult-to-model phenomena. Therefore, our solution is also serviceable in developing an economical and physically-interpretable integrable approach that gets the best of both worlds.

REFERENCES

[1] H.-S. Chung and J. Jia, "Efficient photometric stereo on glossy surfaces with wide specular lobes," in *Proc. of Computer Vision and Pattern Recognition*, 2008, pp. 1–8.

[2] A. S. Georghiades, "Incorporating the Torrance and Sparrow model of reflectance in uncalibrated photometric stereo," in *Proc. of Computer Vision and Pattern Recognition*, 2003, pp. 816–823.

[3] D. B. Goldman, B. Curless, A. Hertzmann, and S. M. Seitz, "Shape and spatially-varying BRDFs from photometric stereo," *IEEE Transactions on Pattern Analysis and Machine Intelligence*, vol. 32, no. 6, pp. 1060–1071, 2010.

[4] H. Santo, M. Samejima, Y. Sugano, B. Shi, and Y. Matsushita, "Deep photometric stereo network," in *Proc. of International Conference on Computer Vision Workshop*, 2017, pp. 501–509.

[5] Z. Hui and A. C. Sankaranarayanan, "A dictionary-based approach for estimating shape and spatially-varying reflectance," in *Proc. International Conference on Computational Photography (ICCP)*, 2015, pp. 1–9.

[6] G. Chen, K. Han, and K.-Y. K. Wong, "PS-FCN: A flexible learning framework for photometric stereo," in *Proc. of European Conference on Computer Vision*, 2018, pp. 3–18.

[7] K. E. Torrance and E. M. Sparrow, "Theory for off-specular reflection from roughened surfaces," *Journal of the Optical Society of America*, vol. 57, no. 9, pp. 1105–1112, 1967.

[8] R. L. Cook and K. E. Torrance, "A reflectance model for computer graphics," *ACM Transactions on Graphics (Proc. of ACM SIGGRAPH)*, vol. 1, no. 1, pp. 7–24, 1982.

[9] Z. Dong, B. Walter, S. Marschner, and D. P. Greenberg, "Predicting appearance from measured microgeometry of metal surfaces," *ACM Transactions on Graphics*, vol. 35, no. 1, p. 9, 2015.

[10] M. M. Bagher, J. Snyder, and D. Nowrouzezahrai, "A non-parametric factor microfacet model for isotropic BRDFs," *ACM Transactions on Graphics*, vol. 35, no. 5, p. 159, 2016.

[11] B. Walter, S. R. Marschner, H. Li, and K. E. Torrance, "Microfacet models for refraction through rough surfaces," in *Proc. of the 18th Eurographics conference on Rendering Techniques*, 2007, pp. 195–206.

[12] M. Ashikhmin and P. Shirley, "An anisotropic Phong BRDF model," *Journal of graphics tools*, vol. 5, no. 2, pp. 25–32, 2000.

[13] L. Chen, Y. Zheng, B. Shi, A. Subpa-Asa, and I. Sato, "A microfacet-based reflectance model for photometric stereo with highly specular surfaces," in *Proc. of International Conference on Computer Vision*, 2017.

[14] B. T. Phong, "Illumination for computer generated pictures," *Communications of the ACM*, vol. 18, no. 6, pp. 311–317, 1975.

[15] J. F. Blinn, "Models of light reflection for computer synthesized pictures," in *Proc. of ACM SIGGRAPH*, vol. 11, no. 2, 1977, pp. 192–198.

[16] E. P. Lafortune and Y. D. Willems, "Using the modified Phong reflectance model for physically based rendering," 1994.

[17] E. P. Lafortune, S.-C. Foo, K. E. Torrance, and D. P. Greenberg, "Non-linear approximation of reflectance functions," in *Proc. of the 24th Annual Conference on Computer Graphics and Interactive Techniques*, 1997, pp. 117–126.

[18] B. Smith, "Geometrical shadowing of a random rough surface," *IEEE Transactions on Antennas and Propagation*, vol. 15, no. 5, pp. 668–671, 1967.

[19] J. T. Kajiya, "Anisotropic reflection models," *Proc. of ACM SIGGRAPH*, vol. 19, no. 3, 1985.

[20] M. Oren and S. K. Nayar, "Generalization of Lambert's reflectance model," in *Proc. of the 21st Annual Conference on Computer Graphics and Interactive Techniques*, 1994, pp. 239–246.

[21] G. J. Ward, "Measuring and modeling anisotropic reflection," *Proc. of ACM SIGGRAPH*, vol. 26, no. 2, pp. 265–272, 1992.

[22] P. Beckmann and A. Spizzichino, "The scattering of electromagnetic waves from rough surfaces," *Artech Print on Demand*, 1987.

[23] M. Ashikhmin and S. Premoze, "Distribution-based BRDFs," *Unpublished Technical Report, University of Utah*, vol. 2, p. 6, 2007.

[24] B. Burley and W. D. A. Studios, "Physically-based shading at Disney," in *Proc. of ACM SIGGRAPH*, 2012, pp. 1–7.

[25] L.-Q. Yan, M. Hašan, S. Marschner, and R. Ramamoorthi, "Position-normal distributions for efficient rendering of specular microstructure," *ACM Transactions on Graphics*, vol. 35, no. 4, p. 56, 2016.

[26] L.-Q. Yan, M. Hašan, W. Jakob, J. Lawrence, S. Marschner, and R. Ramamoorthi, "Rendering glints on high-resolution normal-mapped specular surfaces," *ACM Transactions on Graphics*, vol. 33, no. 4, p. 116, 2014.

[27] A. Gardner, C. Tchou, T. Hawkins, and P. Debevec, "Linear light source reflectometry," in *ACM Transactions on Graphics*, vol. 22, no. 3, 2003, pp. 749–758.

[28] W. Matusik and M. Brand, "A data-driven reflectance model," *ACM Transactions on Graphics (Proc. of ACM SIGGRAPH)*, vol. 22, no. 3, pp. 759–769, 2003.

[29] A. Ngan, F. Durand, and W. Matusik, "Experimental analysis of BRDF models." *Rendering Techniques*, vol. 2005, no. 16, p. 2, 2005.

[30] Y. Dong, J. Wang, X. Tong, J. Snyder, Y. Lan, M. Ben-Ezra, and B. Guo, "Manifold bootstrapping for SVBRDF capture," in *ACM Transactions on Graphics (Proc. of ACM SIGGRAPH)*, vol. 29, no. 4, 2010, p. 98.

[31] A. Bilgili, A. Öztürk, and M. Kurt, "A general BRDF representation based on tensor decomposition," in *Computer Graphics Forum*, vol. 30, no. 8, 2011, pp. 2427–2439.

[32] J. Lawrence, S. Rusinkiewicz, and R. Ramamoorthi, "Efficient BRDF importance sampling using a factored representation," in *ACM Transactions on Graphics*, vol. 23, no. 3, 2004, pp. 496–505.

[33] E. Heitz, "Understanding the masking-shadowing function in microfacet-based BRDFs," *Journal of Computer Graphics Techniques*, vol. 3, no. 2, pp. 32–91, 2014.

[34] C. Schlick, "An inexpensive BRDF model for physically-based rendering," in *Computer Graphics Forum*, vol. 13, no. 3, 1994, pp. 233–246.

[35] B. Walter, Z. Dong, S. Marschner, and D. P. Greenberg, "The ellipsoid normal distribution function," *Supplementary material*, vol. http://www.cs.cornell.edu/Projects/metalappearance/, 2016.

[36] T. S. Trowbridge and K. P. Reitz, "Average irregularity representation of a rough surface for ray reflection," *Journal of the Optical Society of America*, vol. 65, no. 5, pp. 531–536, 1975.

[37] G. Nam, J. H. Lee, H. Wu, D. Gutierrez, and M. H. Kim, "Simultaneous acquisition of microscale reflectance and normals," *ACM Transactions on Graphics*, vol. 35, no. 6, 2016.

[38] B. K. Horn, "Shape from shading: A method for obtaining the shape of a smooth opaque object from one view," 1970.

[39] R. J. Woodham, "Photometric method for determining surface orientation from multiple images," *Optical engineering*, vol. 19, no. 1, pp. 139–144, 1980.

[40] P. N. Belhumeur and D. J. Kriegman, "What is the set of images of an object under all possible illumination conditions?" *International Journal of Computer Vision*, vol. 28, no. 3, pp. 245–260, 1998.

[41] R. Basri and D. W. Jacobs, "Lambertian reflectance and linear subspaces," *IEEE Transactions on Pattern Analysis and Machine Intelligence*, vol. 25, no. 2, pp. 218–233, 2003.

[42] R. Ramamoorthi, "Analytic PCA construction for theoretical analysis of lighting variability in images of a Lambertian object," *IEEE Transactions on Pattern Analysis and Machine Intelligence*, vol. 24, no. 10, pp. 1322–1333, 2002.

[43] L. Wu, A. Ganesh, B. Shi, Y. Matsushita, Y. Wang, and Y. Ma, "Robust photometric stereo via low-rank matrix completion and recovery," in *Proc. of Asian Conference on Computer Vision*, 2010, pp. 703–717.

[44] S. Ikehata, D. Wipf, Y. Matsushita, and K. Aizawa, "Robust photometric stereo using sparse regression," in *Proc. of Computer Vision and Pattern Recognition*, 2012, pp. 318–325.

[45] S.Ikehata, D. Wipf, Y. Matsushita, and K. Aizawa, "Photometric stereo using sparse bayesian regression for general diffuse surfaces," *IEEE Transactions on Pattern Analysis and Machine Intelligence*, vol. 36, no. 9, pp. 1816–1831, 2014.

[46] S. Tozza, R. Mecca, M. Duocastella, and A. D. Bue, "Direct differential photometric stereo shape recovery of diffuse and specular surfaces," *Journal of Mathematical Imaging and Vision*, vol. 56, pp. 57–76, 2016.

[47] S. K. Nayar, K. Ikeuchi, and T. Kanade, "Surface reflection: physical and geometrical perspectives," *IEEE Transactions on Pattern Analysis and Machine Intelligence*, vol. 13, no. 7, pp. 611–634, 1991.

[48] A. Hertzmann and S. M. Seitz, "Example-based photometric stereo: Shape reconstruction with general, varying brdfs," *IEEE Transactions on Pattern Analysis and Machine Intelligence*, vol. 27, no. 8, pp. 1254–1264, 2005.

[49] N. G. Alldrin and D. J. Kriegman, "Toward reconstructing surfaces with arbitrary isotropic reflectance: A stratified photometric stereo approach," in *Proc. of International Conference on Computer Vision*, 2007, pp. 1–8.

[50] B. Shi, P. Tan, Y. Matsushita, and K. Ikeuchi, "Elevation angle from reflectance monotonicity: Photometric stereo for general isotropic reflectances," in *Proc. of European Conference on Computer Vision*, 2012, pp. 455–468.

[51] T. Higo, Y. Matsushita, and K. Ikeuchi, "Consensus photometric stereo," in *Proc. of Computer Vision and Pattern Recognition*, 2010, pp. 1157–1164.

[52] Y. Sato and K. Ikeuchi, "Temporal-color space analysis of reflection," *Journal of Optical Society of America A*, vol. 11, no. 11, pp. 2990–3002, 1994.

[53] S. P. Mallick, T. E. Zickler, D. J. Kriegman, and P. N. Belhumeur, "Beyond Lambert: Reconstructing specular surfaces using color," in *Proc. of Computer Vision and Pattern Recognition*, vol. 2, 2005, pp. 619–626.

[54] N. Alldrin, T. Zickler, and D. Kriegman, "Photometric stereo with non-parametric and spatially-varying reflectance," in *Proc. of Computer Vision and Pattern Recognition*, 2008, pp. 1–8.

[55] Z. Wu and P. Tan, "Calibrating photometric stereo by holistic reflectance symmetry analysis," in *Proc. of Computer Vision and Pattern Recognition*, 2013, pp. 1498–1505.

[56] S. Ikehata and K. Aizawa, "Photometric stereo using constrained bivariate regression for general isotropic surfaces," in *Proc. of Computer Vision and Pattern Recognition*, 2014, pp. 2179–2186.

[57] T. Taniai and T. Maehara, "Neural inverse rendering for general reflectance photometric stereo," in *Proc. of International Conference on Machine Learning*, 2018.

[58] B. Shi, Z. Mo, Z. Wu, D. Duan, S.-K. Y. Yeung, and P. Tan, "A benchmark dataset and evaluation for non-Lambertian and uncalibrated photometric stereo," *IEEE Transactions on Pattern Analysis and Machine Intelligence*, vol. 41, no. 2, pp. 271–284, 2019.

[59] B. Shi, P. Tan, Y. Matsushita, and K. Ikeuchi, "Bi-polynomial modeling of low-frequency reflectances," *IEEE Transactions on Pattern Analysis and Machine Intelligence*, vol. 36, no. 6, pp. 1078–1091, 2014.

[60] M. Ashikmin, S. Premože, and P. Shirley, "A microfacet-based BRDF generator," in *Proc. of the 27th annual conference on Computer graphics and interactive techniques*, 2000, pp. 65–74.

[61] R. Goldman, "Curvature formulas for implicit curves and surfaces," *Computer Aided Geometric Design*, vol. 22, no. 7, pp. 632–658, 2005.

[62] G. Vickers, "The projected areas of ellipsoids and cylinders," *Powder Technology*, vol. 86, no. 2, pp. 195–200, 1996.

[63] V. Larsson and K. Åström, "Uncovering symmetries in polynomial systems," in *Proc. of European Conference on Computer Vision*, 2016, pp. 252–267.

[64] M. Pharr, W. Jakob, and G. Humphreys, *Physically based rendering: From theory to implementation*.   Morgan Kaufmann, 2016.

[65] E. A. Rakhmanov, E. Saff, and Y. Zhou, "Minimal discrete energy on the sphere," *Mathematical Research Letters*, vol. 1, no. 6, pp. 647–662, 1994.

[66] Z. Hui and A. C. Sankaranarayanan, "Shape and spatially-varying reflectance estimation from virtual exemplars," *IEEE Transactions on Pattern Analysis and Machine Intelligence*, vol. 39, no. 10, pp. 2060–2073, 2017.

[67] B. Shi, P. Tan, Y. Matsushita, and K. Ikeuchi, "A biquadratic reflectance model for radiometric image analysis," in *Proc. of Computer Vision and Pattern Recognition*, 2012, pp. 230–237.

[68] P. Einarsson, C.-F. Chabert, A. Jones, W.-C. Ma, B. Lamond, T. Hawkins, M. T. Bolas, S. Sylwan, and P. E. Debevec, "Relighting human locomotion with flowed reflectance fields." *Rendering Techniques*, p. 17, 2006.
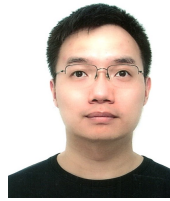
Lixiong Chen received his B.Eng., M.Eng. in Electrical Engineering and the M.Sci. in Computer Science from McGill University in 2009, 2012 and 2018, respectively. Between 2012 and 2014 he worked as an NLP application engineer at Nuance Communications in Montreal. He is currently a researcher in the National Institute of Informatics in Tokyo. His research interests lie in computational photography, computer vision, and mathematical optimization.

Yinqiang Zheng received his Bachelor degree from the Department of Automation, Tianjin University, Tianjin, China, in 2006, Master degree of engineering from Shanghai Jiao Tong University, Shanghai, China, in 2009, and Doctoral degree of engineering from the Department of Mechanical and Control Engineering, Tokyo Institute of Technology, Tokyo, Japan, in 2013. He is currently an associate professor in the National Institute of Informatics, Japan. His research interests include image processing, computer vision, and mathematical optimization.

Boxin Shi is currently a Boya Young Scholar Assistant Professor at Peking University, where he leads the Camera Intelligence Group. Before joining PKU, he did postdoctoral research at MIT Media Lab, Singapore University of Technology and Design, Nanyang Technological University from 2013 to 2016, and worked as a Researcher at the National Institute of Advanced Industrial Science and Technology from 2016 to 2017. He received the B.E. degree from Beijing University of Posts and Telecommunications in 2007, M.E. degree from Peking University in 2010, and Ph.D. degree from the University of Tokyo in 2013. He won the Best Paper Runner-up award at International Conference on Computational Photography 2015. He has served as Area Chairs for ACCV 2018, BMVC 2019, and 3DV 2019.

Art Subpa-asa received the B.E. and M.E. in Computer Engineering from Chulalongkorn University in 2009 and 2011, and Ph.D. in information processing from the Tokyo Institute of Technology in 2018, respectively. He is currently a researcher in the National Institute of Informatics. His research interests include computational photography of global illumination and acquisition system.

Imari Sato received the B.S. degree in policy management from Keio University in 1994. After studying at the Robotics Institute of Carnegie Mellon University as a visiting scholar, she received the M.S. and Ph.D. degrees in interdisciplinary Information Studies from the University of Tokyo in 2002 and 2005, respectively. In 2005, she joined the National Institute of Informatics, where she is currently a professor. Her primary research interests are in the fields of computer vision (physics-based vision, image-based modeling) and Computer Graphics (image-based rendering, augmented reality). She has received various research awards, including IPSJ Nagao Special Researcher award (2010), The Young Scientists Prize from The Commendation for Science and Technology by the Minister of Education, Culture, Sports, Science and Technology (2009), and Microsoft Research Japan New Faculty award (2011).